Development of advanced measuring instruments based on SQUID sensors for laboratory and industrial applications

R. Nagendran, N. Thirumurugan, N. Chinnasamy and M. P. Janawadkar

The design and development of Superconducting QUantum Interference Devices (SQUID)-based measuring systems using the indigenously developed SQUID sensors and the associated readout electronics is described in detail. The high-field SQUID magnetometer has a sensitivity of 1.2 $\times 10^{-7}$ emu of magnetic moment. It incorporates several novel features such as a variable temperature regulator based on impedance capillary for achieving excellent temperature control, and the use of a novel input circuit that utilizes two SQUID sensors with different strengths of input signal coupling in order to allow a user-selectable trade-off between high-resolution measurements with a lower dynamic range and low-resolution measurements with a higher dynamic range to permit measurement of magnetization of samples with low as well as high values of magnetic moment. SQUID-based system for nondestructive evaluation of materials harnesses the low-frequency sensitivity of the SQUID sensors for the detection of deep subsurface defects not detectable by the conventional eddy current techniques owing to skin depth limitations. The system is based on a precision X–Y–θ scanner with a position resolution of 50 μm, custom designed indigenously for this application and has been extensively used for studies on the frequency and depth dependence of the magnetic anomalies associated with the perturbation of the flow of eddy currents in the vicinity of the defects.

For more than two decades, Superconducting QUantum Interference Devices (SQUIDs) have played a key role in the development of advanced measuring systems suitable for a wide spectrum of applications such as laboratory measurements, biomagnetism, non-destructive evaluation (NDE), geophysical explorations, etc. The unparalleled sensitivity of SQUID sensor (10 fT) yields measureable voltage output for extremely small changes in input magnetic flux, enabling SQUID device to be used as a transducer for tracking magnetic flux changes with a sensitivity superior to that offered by any other sensor technology. The systems based on SQUID sensors offer a wide bandwidth (from near DC to hundreds of kHz), wide dynamic range (>100 dB) and an intrinsically quantitative response. The unprecedented sensitivity of SQUID sensor together with the use of superconducting pick-up loops (used as input circuits) enables one to realize practical measuring instruments for the measurement of extremely weak magnetic signals with a high sensitivity. The bare SQUID sensor produces a periodic output voltage with the periodicity of one flux quantum Φ_0 (= $h/2e$ = 2.07 × 10^{-15} Wb) for a linearly varying input flux. To utilize SQUID sensors for real applications, flux locked loop (FLL) readout electronics has been developed indigenously to linearize the periodic output voltage of SQUID. Using SQUID sensor and its associated readout electronics, it is possible to detect a change in the applied magnetic flux whose magnitude is much less than one flux quantum. SQUID sensors can measure any physical quantity that can be converted into magnetic flux, and have been used, for example, for the measurement of magnetic field, magnetic field gradient, magnetic susceptibility, electric current, voltage, pressure, mechanical displacement, etc. with an unprecedented sensitivity. This note describes the successful design and development of a high-field SQUID magnetometer, which is being utilized for physics research, as well as the development of a SQUID-based system for NDE, which is being utilized in engineering applications. The high-field SQUID magnetometer system has been extensively characterized, calibrated and used for magnetization measurements up to a magnetic field of 7 T and the temperature of the sample can be varied from 4.2 to 300 K, with user-selectable rate of ramping during cool-down/warm-up and a temperature stability of 2 mK at 10 K and 10 mK at 200 K. The sensitivity of the system is shown to be better than 1.2×10^{-7} emu at relatively low magnetic fields and ~10^{-5} emu at high fields. Similarly, the SQUID-based NDE system has been used for the measurement of subsurface flaws by inducing eddy currents in conducting materials at relatively low frequencies. Detailed experimental studies have been carried out for the determination of optimum eddy current excitation frequencies for flaws located at different depths below the top surface of an aluminum plate. This system has also been used for the monitoring of the progressive transformation of extremely low content of magnetic δ-ferrite phase into nonmagnetic phases in the 316L(N) stainless steel weldment specimens subjected to low cycle fatigue (LCF) at high temperatures.

SQUID sensors: principle of operation

The SQUID is basically a superconducting sensor which operates below the transition temperature (T_c) of the superconducting materials used for fabrication of the device. The basic phenomena governing the operation of SQUID devices are flux quantization in superconducting loops and the Josephson effect (Figure 1). As detailed descriptions are available in the literature[1,2], a brief description

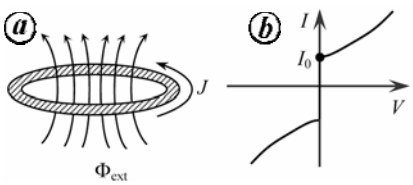

Figure 1. ***a***, Flux quantization. ***b***, Non-hysteretic *I–V* characteristic of a resistively shunted Josephson junction.

of the working principle of the SQUID sensor is included here to make the note self-contained.

Flux quantization refers to the fact that the total flux linked with a superconducting loop is always constrained to be an integral multiple of a flux quantum (Φ_0).

$$\Phi_{tot} = \Phi_{ext} + LJ = n\Phi_0, \quad (1)$$

where Φ_{ext} is the externally applied magnetic flux, L the self-inductance of the superconducting loop, J the screening current induced in the superconducting loop because of the application of the external magnetic flux and n is an integer. The Josephson effect refers to the ability of two weakly coupled superconductors to sustain at zero voltage a supercurrent associated with the transport of Cooper pairs, whose magnitude depends on the phase difference between the two superconductors.

$$I = I_0 \sin \delta\varphi, \quad (2)$$

where I_0 is the maximum current the junction can sustain without developing any voltage and is known as the critical current of the Josephson junction, and $\delta\varphi$ the phase difference between the two weakly coupled superconductors. When two superconductors are separated by a thin oxide barrier (tunnel junction), the establishment of tunnelling-assisted phase coherence leads to the Josephson effect; *I–V* characteristic of such a tunnel junction shows hysteretic behaviour due to non-negligible value of junction capacitance. This hysteresis is, however, undesirable and can be eliminated by shunting the junction with appropriate on-chip thin film resistor to provide sufficient damping of the phase dynamics. A DC SQUID consists of two such non-hysteretic Josephson junctions connected by a superconducting loop.

To describe the operation of the DC SQUID, we assume that the bias current I_b is swept from zero to a value above the critical current ($2I_0$) of the two junctions. An external magnetic flux varying slowly in time is applied perpendicular to the plane of the loop; its characteristic frequency is much lower than the frequency of the Josephson oscillations at the chosen value of the bias current. When the external applied magnetic flux is zero (or $n\Phi_0$, n is an integer), there is no screening current induced in the superconducting loop and the bias current I_b simply divides equally between the two junctions assuming the SQUID to be symmetric. When the external magnetic flux Φ_{ext} is applied, the requirement of flux quantization generates a screening current $J = -(\Phi_{ext} - n\Phi_0)/L_s$, where L_s is the inductance of the SQUID loop and n an integer which makes the value of $n\Phi_0$ nearest to the applied flux Φ_{ext}. Any inductance associated with the two Josephson junctions is negligibly small compared to the inductance of SQUID loop. The screening current induced in SQUID loop adds to the bias current flowing through junction 1 and subtracts from that flowing through junction 2. When junction 1 reaches its critical current $I_0 = I_b/2 + J$, the current flowing in junction 2 is $(I_0 - 2J)$, and the total current flowing in SQUID is $(2I_0 - 2J)$. At this point SQUID switches to the non-zero voltage state. When the applied flux is increased to $\Phi_0/2$, the screening current J reaches a value of $\Phi_0/2L_s$ and the critical current falls to $(2I_0 - \Phi_0/L_s)$ as shown in Figure 2 *b*. When the flux Φ_{ext} is increased further, SQUID makes a transition from the flux state $n = 0$ to the state $n = 1$; J changes its sign and reaches zero again when Φ_{ext} becomes equal to Φ_0. At this point, the critical current of SQUID is restored to its maximum value of $2I_0$. In this way the critical current oscillates as a function of Φ_{ext}. If we bias SQUID with a DC current greater than the critical current of the two Josephson junctions, the voltage developed across SQUID oscillates with a period of Φ_0 when the input magnetic flux steadily increases. Thus, SQUID produces output voltage in response to a small input flux $\delta\Phi(<<\Phi_0)$, and is effectively a flux-to-voltage transducer. The voltage swing δV produced at the output of the SQUID when the flux changes from $n\Phi_0$ to $(n + 1/2)\Phi_0$ is known as the modulation depth of SQUID. The modulation depth of a typical low T_c DC SQUID based on Nb/AlO_x/Nb Josephson junctions is ~20 to 30 μV. The usable voltage swing δV is maximum for bias currents a little above the maximum critical current of SQUID, and during operation SQUID is tuned to the bias current at which the modulation depth is a maximum.

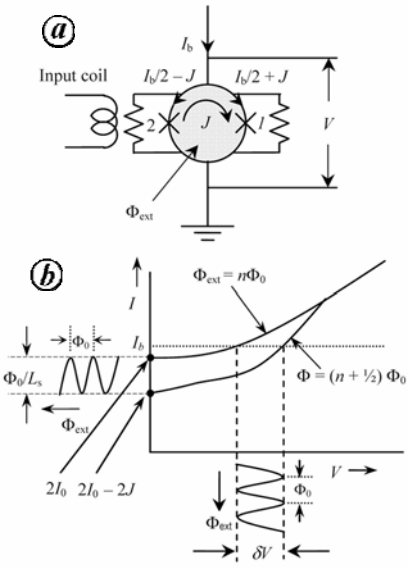

Figure 2. ***a***, DC SQUID. ***b***, *I–V* characteristic of the DC SQUID with application of input magnetic flux.

Flux locked loop readout electronics

The periodic output voltage of SQUID allows it to be operated in a small signal mode around the optimum working point, but the linearity of response is limited to a flux range much less than $\Phi_0/4$. The small signal readout can only be used when the amplitude of variation of the magnetic flux signal is limited to the linear range around the working point ($<\Phi_0/4$). However, in most applications, the signal flux which is to be measured varies from a fraction of a flux quantum to several hundreds of flux quanta. Therefore, the measurement system based on SQUID sensor should be designed to provide a wide dynamic range as required in any application. In order to linearize the periodic output voltage, SQUID should be operated in a feedback loop as a null detector of magnetic flux; the voltage at the output of the readout electronics will then be proportional to the input signal flux.

In order to suppress the $1/f$ noise and DC drifts in the preamplifier, the signal of interest is shifted to frequencies well above the threshold of $1/f$ noise using high-frequency flux modulation scheme as illustrated in Figure 3. In this scheme, the signal flux, $\delta\Phi_{sig}$, which is to be measured is modulated by a high-frequency carrier flux $\Phi_m(t)$. The sinusoidal modulation flux, $\Phi_m(t)$ of frequency f_m with a peak-to-peak value of nearly $\Phi_0/2$ is applied to SQUID. When there is no

applied signal flux or the applied input flux is $n\Phi_0$, SQUID produces output voltage with a frequency twice that of the modulation flux $\Phi_m(t)$, and there is no component at the modulation frequency present in this output. When this voltage output is fed to a lock-in detector referenced to f_m, the output of the lock-in detector is zero. On the other hand, when the applied signal flux is $(n + 1/4)\Phi_0$, SQUID output voltage has a component at frequency f_m which is in-phase with the carrier frequency and the output of the lock-in detector is maximum. Similarly, when the signal flux is $(n - 1/4)\Phi_0$, SQUID output voltage has a component at frequency f_m, which is out of phase with the carrier and the output of the lock-in detector has a maximum negative value. Thus, as one increases the flux from $n\Phi_0$ to $(n + 1/4)\Phi_0$, the output from the lock-in detector referenced to f_m steadily increases from zero to a maximum positive value; if instead the flux is decreased from $n\Phi_0$ to $(n - 1/4)\Phi_0$, the output from the lock-in detector referenced to f_m decreases from zero to a maximum negative value. The lock-in output is integrated and fed back to the same coil as that used for flux modulation via a feedback resistor. The signal flux $\delta\Phi_{sig}$ applied to SQUID produces an output of $-\delta\Phi_{sig}$ from the feedback loop to maintain a constant flux in SQUID, while producing an output voltage across the feedback resistor which is proportional to $\delta\Phi_{sig}$.

The schematic diagram of the FLL readout electronics is shown in Figure 4. In order to achieve a low system noise, it is necessary to match the output impedance of SQUID device and input impedance of the preamplifier. LT1028 (Linear Technology) was chosen to construct the preamplifier. The spectral densities of the voltage noise (e_n) and current noise (i_n) of the preamplifier at a frequency of 100 kHz are specified by the manufacturer to be about 0.9 nV/√Hz and 1 pA/√Hz respectively. The optimum input impedance (e_n/i_n) of the preamplifier is, therefore, about 900 Ω. Since the dynamic resistance of the SQUID at its optimum bias point is about 1 Ω, one requires a coupling circuit with an impedance transformation of about 900 for effective signal extraction from the SQUID. In addition, the bandwidth of the coupling circuit should be as large as possible to extract the 100 kHz modulation signal without attenuation. For this, a room-temperature step-up transformer with a turns ratio of 30 has been fabricated and used as an impedance matching circuit. The room-temperature transformer consists of 10 turns of 24 SWG copper wire as primary coil and 300 turns of 28 SWG copper wire as secondary coil wound on a toroidal ferrite core. The inner and outer diameters of the toroidal core are 10 and 18 mm respectively. The step-up transformer is housed in the preamplifier box and the preamplifier is mounted at the top of SQUID insert. The SQUID is biased with an optimum DC bias current, I_b, to get maximum voltage modulation from SQUID sensor. The magnetic flux, which is to be measured (in actual measurements) is applied to the input coil of SQUID, which is inductively coupled to SQUID loop via the mutual inductance, $M_i \propto \sqrt{L_i L_s}$, where L_i is the self-inductance of the input coil and L_s the self-inductance of SQUID loop. The signal flux is modulated by a 100 kHz sinusoidal flux whose peak-to-peak amplitude is less than $\Phi_0/2$. The modulated output voltage is stepped up by the impedance matching transformer and further amplified by a two-stage amplifier with sufficient gain and fed to the signal input channel of the analog multiplier. The modulated output is phase-sensitively detected with respect to the reference signal supplied from the same 100 kHz oscillator to the reference input channel of the analog multiplier. The output of the analog multiplier is integrated and fed back as a current to the feedback coil in order to counterbalance the signal flux applied to SQUID. The voltage, V_f developed across the feedback resistor R_f is proportional to the input flux and the transfer function of the system $(\partial V_{FLL}/\partial\Phi_{sig})$ is given by (R_f/M_f), where R_f is the feedback resistance and M_f is the mutual inductance between the feedback coil and SQUID[3]. As an illustration of the typical voltage waveforms expected, Figure 5 shows the integrator output for a sinusoidally varying input flux at various frequencies and amplitudes when the feedback switch is open. As shown in Figure 5, the output waveform from the SQUID varies as the frequency and

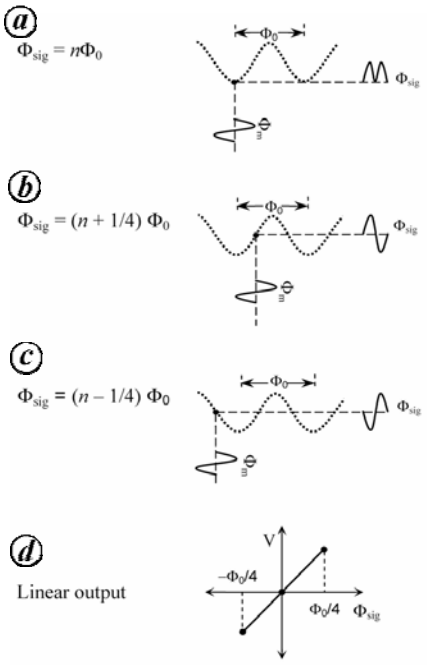

Figure 3. Schematic representation of the flux modulation scheme.

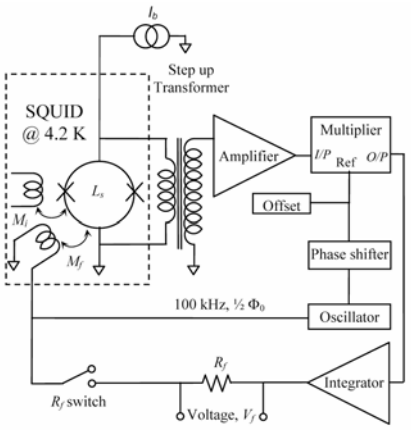

Figure 4. Schematic diagram of the flux locked loop electronics with flux modulation scheme.

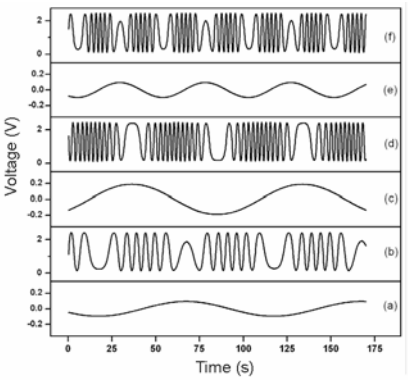

Figure 5. The integrator output voltage waveforms (upper trace) and the corresponding applied flux signal (lower trace). Note the changes as the amplitude and frequency of the signal flux are changed.

amplitude of the input signal is varied. Figure 5 *a* shows the sinusoidal input flux applied to the SQUID at a frequency of 10 mHz with an amplitude equivalent to 6.25 Φ_0. Figure 5 *b* shows the corresponding integrator output. Figure 5 *c* and *d* shows a sinusoidal input flux applied at a frequency of 10 mHz with an amplitude equivalent to 12.5Φ_0 and the corresponding integrator output respectively. Figure 5 *e* and *f* shows a sinusoidal input flux applied to the SQUID at a frequency of 20 mHz with an amplitude equivalent to 6.25 Φ_0 and the corresponding integrator output respectively. These waveforms illustrate the folding of the SQUID output voltage when the flux coupled to SQUID exceeds $\Phi_0/2$. When the feedback switch is closed, the feedback flux at SQUID cancels the input flux and the system uses SQUID as a null detector of magnetic flux. The voltage developed across the feedback resistor is proportional to the applied input flux and the time variation of this voltage is an exact replica of that of the input signal flux coupled to SQUID. The system gain can be varied by simply varying the value of the feedback resistor. The figures of merit of SQUID system with FLL readout electronics are the flux noise, slew rate and bandwidth; these values are listed in Table 1 for the system developed in our laboratory.

SQUID-based measuring systems

There are some important issues to be considered while building measuring instruments based on SQUID sensors. Since the sensing area of SQUID is small (typically 10^{-2} mm^2), direct sensing of the signal flux leads to poor field resolution. The field resolution can be improved to some extent by increasing the effective area of the SQUID sensor[4]. A better way to increase the field resolution, however, involves the use of superconducting pick-up loop with larger area in the form of a magnetometer or a gradiometer connected to the on-chip integrated multi-turn input coil which is magnetically tightly coupled to SQUID. The noise energy coupled to SQUID is minimum only when $L_i = L_p$, where L_i and L_p are the inductances of the input coil and pick-up loop respectively. For a typical low-T_c DC SQUID and radius of the pick-up loop $r_p \sim 10$ mm, one can expect the white magnetic field noise of the order of 1 fT/√Hz. Such sensitivities can only be utilized fully inside a superconducting shield or in a magnetically shielded room. In unshielded environments, fluctuations in the earth's magnetic field, local fields at power-line frequency and disturbances due to strong sources such as rotating machinery will dominate the applied magnetic field to SQUID. For sensitive measurements using SQUID sensors, like the measurement of biomagnetic fields and high-resolution measurement of magnetic susceptibility, the use of gradiometers for rejection of distant sources of noise is almost inevitable. Figure 6 *b* shows the principle of a first-derivative, axial gradiometer consisting of two pick-up loops of equal turn areas connected in series; the loops are wound in opposition and are separated by the baseline, *b*. A uniform magnetic field B_z ideally induces zero net screening current into the two loops, and hence couples no net flux to SQUID. A gradient $\partial B_z/\partial z$, on the other hand, induces a net screening current in the gradiometer, which is transferred to the input coil and a corresponding flux is inductively coupled to SQUID. Figure 6 *c* shows the configuration of the second-derivative axial gradiometer consisting of two first-derivative gradiometers wound in opposite direction. For uniform magnetic field and first-order field gradient, the net screening current induced in the second-order gradiometer is zero. The second-derivative field gradient $\partial^2 B_z/\partial z^2$ induces screening current in such a gradiometer and couples a net flux to SQUID.

Table 1. Benchmarks of the SQUID system

Flux noise ($\mu\Phi_0/\sqrt{\text{Hz}}$)	Slew rate (Φ_0/s)	Bandwidth (kHz)
10	5×10^5	10

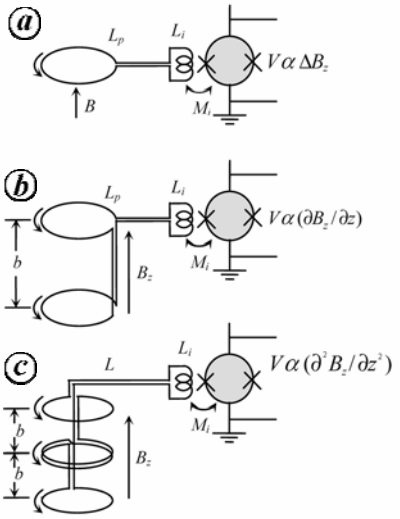

Figure 6. Pick-up loop configuration with different geometries connected to the input coil of the SQUID magnetometer (***a***), first-order gradiometer (***b***) and second-order gradiometer (***c***).

The SQUID-based measuring system has to be designed considering the nature of the signal source of interest. In some cases the signal source may be exposed to high temperature, high magnetic fields like magnetization measurements. In some other cases like nondestructive testing, biomagnetism, geophysics, SQUID microscope, etc. the signal source may have to be kept at room temperature and is often outside the cryostat.

In magnetization measurements, the sample size is small and the signal strength is weak; the sample, therefore, has to be oscillated across the superconducting gradiometer. To ensure that the magnetizing field is homogeneous over the range of sample oscillations, a short baseline is preferred. But in the case of NDE measurements, the specimen may be large in size and it cannot be oscillated across the pick-up loop. In this case, a gradiometer with longer baseline may enhance the signal-to-noise ratio.

Construction of high-field SQUID magnetometer

In this section, development of the high-field SQUID magnetometer is briefly described. Its design, fabrication, integration, testing and calibration have been described in detail elsewhere[5]. SQUID magnetometers with first-order gradiometer and various magnetic field capabilities have been described by several workers[6–18]. The present design is modular and all the sub-systems have been fabricated in the form of separate modules in order to simplify the assembly and to facilitate maintenance. The system consists of four major modules: (i) sample chamber with variable temperature regulator (VTR) for varying the sample temperature from one value to another with uniform rates of heating and cooling

and to maintain the sample temperature with a high stability; (ii) superconducting shield chamber for maintaining stable magnetic field across the superconducting gradiometric pick-up loop; (iii) SQUID sensor and its input circuit in the form of second-order gradiometer, and (iv) stepper motor-driven sample transport assembly for oscillating the sample across the pick-up loop to record SQUID output signal with respect to the positional coordinates of the sample. In this set-up, several novel features have been incorporated such as an impedance chamber-based VTR for achieving uniform rates of cooling and heating, and for maintaining the sample temperature constant with a high stability, whenever desired, and the use of two different SQUID sensors with different strengths of input signal coupling in order to improve the overall dynamic range of the system.

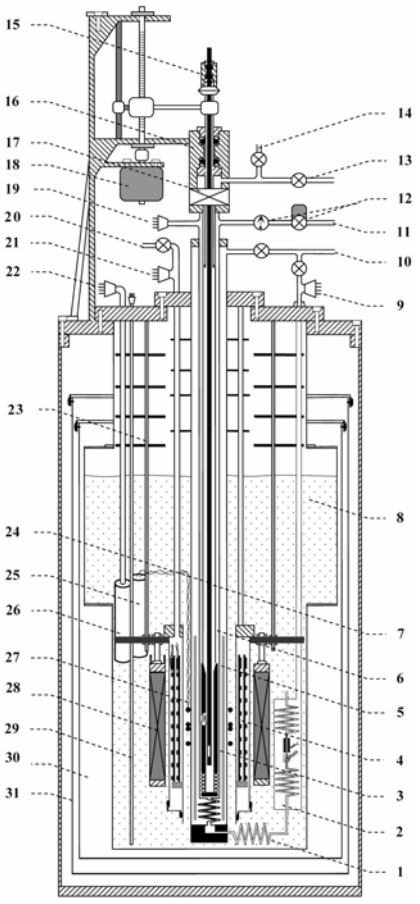

Figure 7. Detailed cross-sectional view of the high-field SQUID magnetometer. 1, Heat exchanger; 2, Impedance chamber; 3, OHFC copper block; 4, NbTi shields; 5, Thermal isolation vacuum chamber; 6, VTR chamber; 7, Sample chamber; 8, Liquid helium reservoir; 9, Electrical feedthrough for impedance chamber; 10, Evacuation port for thermal isolation and impedance chamber; 11, Pumping line for helium; 12, Manometer and throttle valve; 13, Pumping line for sample loading; 14, Helium exchange gas; 15, Wilson seal for sample loading; 16, Wilson seal for sample movement; 17, Gate valve; 18, Stepper motor; 19, Port for heater and thermometer (sample); 20, Evacuation port for shield chamber; 21, Port for heater and thermometer (NbTi shields); 22, Port for SQUID; 23, Radiation baffles; 24, Sample rod; 25, Flux transformer; 26, SQUID; 27, Second order gradiometer pick-up loop; 28, SC Magnet (7 T); 29, Liquid helium level sensor; 30, Thermal radiation shields, and 31, Liquid helium cryostat.

The detailed cross-sectional view of the complete system is shown in Figure 7. The photograph of the high-field SQUID magnetometer set-up is shown in Figure 8. The SQUID magnetometer comprises a liquid helium cryostat with a capacity of 43 litres and a superconducting magnet with a clear bore diameter of 52 mm capable of producing a maximum magnetic field of about 7 T with a field homogeneity of 0.1% over a 10 mm diameter spherical volume (DSV).

The impedance chamber (shown on the right in Figure 7) acts as a precision helium valve to control the incoming flow of cold helium gas into VTR chamber. The liquid helium enters through a fine CuNi capillary tube with an inner diameter of 200 μm and length 80 mm. An electric heater is wound over the fine capillary and a thermometer is mounted over the capillary to monitor and control its temperature. On both sides of the fine capillary, two connecting tubes (inner diameter 1.5 mm) in the form of coils (coil diameter 12 mm and length 40 mm) have been used to reduce the thermal leak between the capillary tube and liquid helium reservoir. The whole arrangement is located inside a vacuum chamber with a vacuum level better than 0.001 mbar. An OFHC copper block with a thermometer and a heater has been mounted in the VTR chamber to monitor and control the desired temperature set by the user. Since the viscosity of helium gas increases with increase in temperature, the incoming helium flow into VTR chamber can be varied just by heating the capillary. The gaseous helium coming out of the capillary is cooled again to a temperature near 4.2 K by the connecting coil, which is in thermal contact with liquid helium. This cold helium gas is allowed to cool the copper block. The cooling rate at the OFHC copper block (sample region) is controlled by controlling the temperature at the capillary and the pressure in VTR chamber.

Figure 8. The high-field SQUID magnetometer set-up.

The VTR has been characterized extensively and a detailed account of its performance has been presented elsewhere[19]. As an illustration of the performance routinely achieved, heating/cooling of the sample at user-desired constant rate of heating/cooling as well as the temperature stabilities typically achieved while maintaining the sample region at different constant temperatures have been shown in Figure 9.

Two superconducting shields in the form of cylindrical tubes machined from a NbTi rod have been used to trap a stable magnetic field and thereby provide a magnetically quiet environment around the sample, despite the ubiquitous magnetic disturbances as well as ripple in the magnet power supply. The inner and outer diameters of the first superconducting shield are 30 and 36 mm, whereas those of the second shield are 33 and 39 mm respectively. The length of both the shields is 210 mm. The superconducting shields are housed in the annular space of the helium tight double-walled vacuum chamber. In order to apply or change the magnetic field in the vicinity of the sample region, the superconducting shields are transformed into the normal state by heating the shields above the superconducting transition temperature. For this purpose, electric heaters have been non-inductively wound using manganin wire with a diameter of 0.1 mm, in grooves machined over the superconducting shields, uniformly with a 4 mm pitch and 0.5 mm depth. To sense the temperature of the shields, insulated NbTi wire has been wound over the shields. The power required to

heat the NbTi shields to a temperature well above 15 K is typically about 1.5–2 W. In order to achieve fast cooling of the shields (from 15 to 4.2 K within 30 s) 2–3 cm^3 of helium gas is permitted into the shield chamber after evacuation.

In the present system, the input circuit is designed to enable a user-selectable trade-off between high-resolution measurements with a lower dynamic range and low resolution measurements with a higher dynamic range in order to permit use of the system to measure magnetization of samples with low as well as high values of magnetic moment. For this, two different SQUID sensors have been used for sensing the magnetization of the sample. One sensor is connected to a highly sensitive input coil system to sense relatively weak magnetic signals with high resolution, and the other one is connected to an input coil system of lower sensitivity to sense strong magnetic signals without allowing the system to reach saturation. The pick-up loop and the flux transformer of the SQUID input circuit used in the present system have been schematically shown in Figure 10. The second-order gradiometric pick-up loop used in the present system consists of three loops ($-n$, $+2n$, $-n$) of 23 mm diameter wound with a 0.1 mm diameter insulated NbTi wire over a cylindrical FRP former. The former has been machined to an outer diameter of 24 mm and grooves have been made with a pitch size of 0.75 mm and depth 0.5 mm. The diameter of each loop is 23 mm and the baseline of the gradiometer is 10.875 mm (these are nominal values estimated from the groove depth and pitch size). The position of the second-order gradiometer is adjusted to ensure that the centre of the gradiometer coincides with the centre of the superconducting magnet and NbTi shields. The leads of the superconducting pick-up loop are twisted and fastened with stycast in the groove machined over a FRP former and connected to the primary coil of the step-down superconducting flux transformer via superconducting contacts. By incorporating this novel input circuit configuration, the dynamic range of the system could be enhanced by two orders of magnitude; the maximum measurable magnetic moment of the sample using SQUIDs with strong and weak coupling is 0.1 and 10 emu respectively.

The measurement process has been fully automated using custom-designed software developed on a LABVIEW platform. The personal computer monitors and controls the electronic instruments as well as various modules of the SQUID magnetometer to perform the magnetization measurements either at constant magnetic field as a function of temperature (M versus T at constant H) or at constant temperature as a function of magnetic field (M versus H at constant T).

The SQUID magnetometer has been calibrated with yttrium iron garnet (YIG) sphere, which is a standard reference material. The value of the magnetic moment of the YIG sphere is certified to be 0.0776 emu at a temperature of 298 K and at a magnetic field of 5000 Oe. The calibration factor was determined by fitting the measured flux profile of the YIG sphere to that expected for a point dipole. The flux profile of the YIG sphere is fitted to the expected flux profile using standard least-square fitting procedures as shown in Figure 11, and the calibration factor is obtained from this fitting.

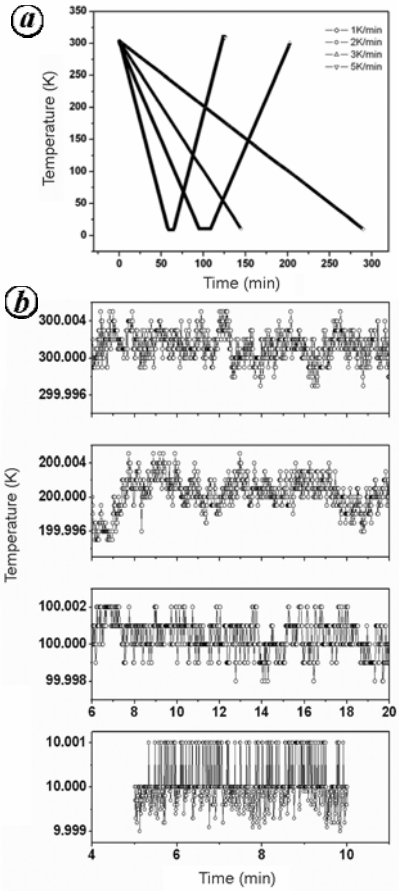

Figure 9. ***a***, Variation of the sample region temperature with uniform rate of heating and cooling set by the user. ***b***, Temperature stabilities recorded experimentally while maintaining a constant temperature of 10, 100, 200 and 300 K in the vicinity of the sample region.

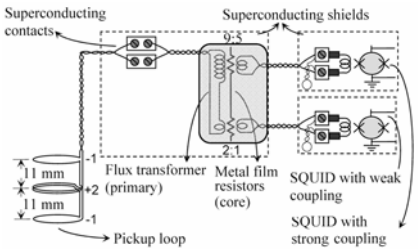

Figure 10. Schematic view of the input circuit employed in the present system using two different SQUID sensors with different strengths of coupling.

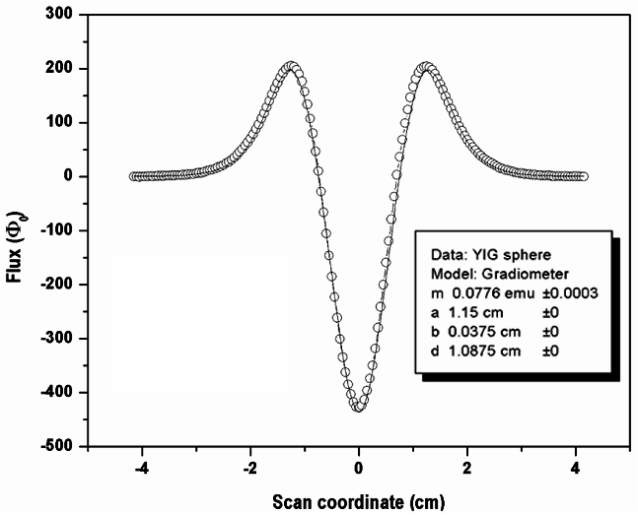

Figure 11. Recorded SQUID output data for the YIG sphere fitted to its magnetic moment value of 0.0776 emu to infer the calibration factor of SQUID magnetometer.

Gd_2O_3 was also used as another reference material for calibration, and the effective magnetic moment of Gd^{3+} could be evaluated from the temperature-dependent magnetization measurements. The temperature-dependent measurements of Gd_2O_3 carried out using the present system show a clear Curie–Weiss-like behaviour (Figure 12). Based on a fit to the linear dependence of the inverse susceptibility χ^{-1} on the temperature, the effective magnetic moment of Gd^{3+} was estimated to be $\mu_{eff} = 7.92 \pm 0.02\ \mu_B$, close to the theoretical value of $7.94\ \mu_B$ for Gd^{3+}, with a Curie–Weiss temperature of $\theta = -15.0$ K, which agrees well with the values reported in the literature. The sensitivity of the system has been estimated to be about 10^{-7} emu at low magnetic fields and about 10^{-5} emu at high magnetic fields, ~7 T.

Construction of SQUID-based NDE system

Conventional eddy current testing is a popular NDE technique for detecting subsurface flaws in conducting structures like aluminum, stainless steel, etc. In this technique, the strength of the eddy current generated in the material by the application of time-varying magnetic field decays exponentially as a function of depth measured from the surface and, therefore, the depth of defect detection is limited by the skin depth of the material. In conventional eddy current testing, the signal decreases if the excitation frequency is decreased in order to increase the skin depth[20]. The system based on SQUID as a detector promises better signal-to-noise ratio at low operating frequencies. Since the sensitivity of SQUID device is independent of the operating frequency from near DC to several kilohertz (white noise regime), it is possible to detect subsurface defects. The pick-up loop can be made of superconducting wire with miniature size; unlike normal metal pick-up loops for which induced voltage is proportional to rate of change of flux, the superconducting pick-up loop directly senses the change in magnetic flux and, hence, its use is crucial in retaining the requisite low-frequency sensitivity. Several groups have successfully utilized this feature to detect subsurface defects not detectable by conventional eddy current techniques[20–25].

Fatigue damage is one of the most important problems for a number of high-temperature components in power plants, particularly in welded regions. A major consideration during the welding of 316L(N) stainless steel is its resistance to hot cracking. The presence of an optimum amount of delta ferrite in the austenitic weld metal is desirable to prevent hot cracking in the weldment. However, the δ-ferrite structure is highly unstable during high-temperature service and transforms to carbides and brittle intermetallic phases, e.g. sigma phase. Since the δ-ferrite is a magnetic phase, one can evaluate the ferrite content by measuring remanent magnetization of the weldment sample.

Here we describe the construction of a SQUID-based NDE system which comprises of a SQUID insert housed in a liquid helium cryostat, precision *XY* scanner for sample movement and data acquisition module to acquire the SQUID output signal with respect to sample coordinates for the flat plate as well as cylindrical samples. The SQUID sensor is housed in an FRP liquid helium cryostat having a capacity of 11.5 litre of liquid helium. The cryostat has a low boil-off rate of under 2.2 litre/day and is designed to have a minimum warm-to-cold distance of 6 mm. The cryostat is equipped with a top-loading clear access of 25 mm diameter for insertion of SQUID probe. The magnetic flux is inductively coupled to SQUID using a first-order gradiometer, which consists of two superconducting loops of 4 mm diameter wound in opposition and separated by a baseline of 40 mm. The set-up was calibrated by measuring the system response to the magnetic field produced by a large circular coil and the calibration constant was inferred to be 20 nT/cm per flux quantum coupled to SQUID. The schematic diagram of the experimental set-up is shown in Figure 13. The photograph of SQUID-based NDE system is shown in Figure 14.

A double 'D' excitation coil at room temperature, placed just below the cryostat, was used to excite eddy currents in the specimen at room temperature. The advantages of using a double 'D' coil for eddy current excitation are described in detail elsewhere[26].

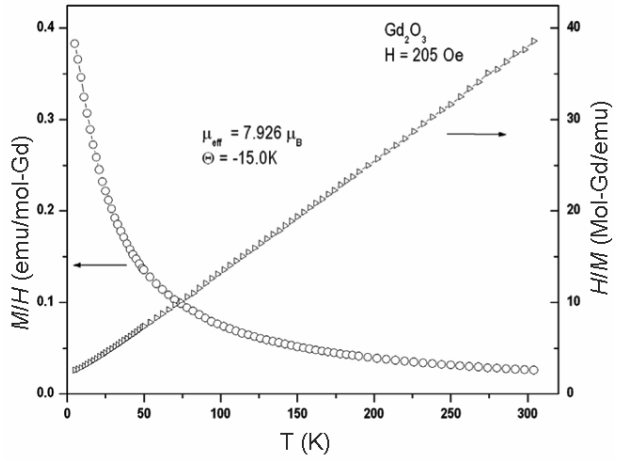

Figure 12. Temperature-dependent susceptibility (*M*/*H*) and inverse susceptibility (*H*/*M*) of Gd_2O_3 sample plotted as a function of temperature.

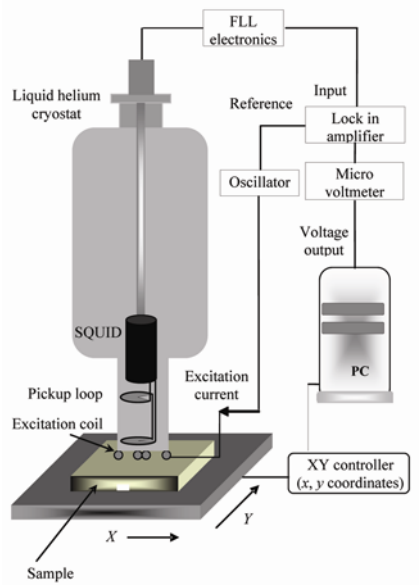

Figure 13. Schematic diagram of the experimental set-up.

The *XY* scanner has been designed for the scanning of flat plate samples with a positional accuracy of 0.025 mm and repeatability of 0.1 mm. The maximum stroke length is about 300 mm along each axis and the scanning speed can be varied from 1 to 50 mm/s. The major components of the *XY* scanner are computer-controlled *XY* stage, supporting platform, which moves smoothly over a frictionless table, and nonmetallic and non-magnetic sample holder. The development of the *XY* scanner has been described in detail elsewhere[27].

A set of aluminum plates with a length of 300 mm, width 200 mm and with different thicknesses ranging between 2 and 12 mm in steps of 2 mm has been fabricated for determination of optimum eddy current excitation frequencies for the detection of flaws located at different depths below the top surface of an aluminum plate. An artificial defect is engineered in a separate 1 mm thick aluminum plate with a defect length of 60 mm and width 0.75 mm to simulate a localized loss of conductor volume in the plate. The length and width of the plate carrying the defect are identical to those of plates without defects. SQUID-based eddy current NDE measurements have been carried out for a stack of aluminum plates with the defect plate located at different depths ranging from 2 to 14 mm (in steps of 2 mm), while keeping the total thickness of the conductor stack at a constant value of 15 mm throughout the experimental studies. The stack of plates was scanned under the SQUID in a direction such that the defect length is perpendicular to the scanning direction. For each scan, eddy currents were induced by passing sinusoidally varying current at an excitation frequency f through the double 'D' excitation coil. Both the real (in-phase) and the imaginary (out-of-phase) components of the resulting SQUID output voltage were measured using the lock-in amplifier and were recorded with respect to the positional coordinates of the defect. For each defect depth, the experiments were repeated at different excitation frequencies ranging between 33 and 853 Hz, in steps of 20 Hz.

Figure 14. The SQUID-based NDE setup.

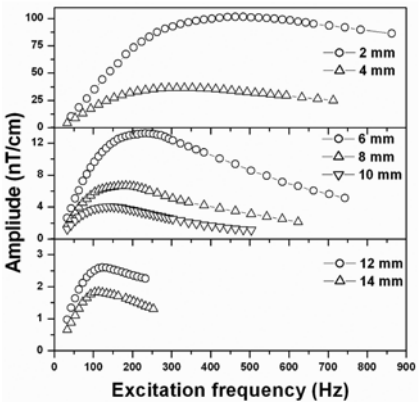

Figure 15. Variation in amplitude of the magnetic anomalies corresponding to defects located at different depths as the excitation frequency is varied.

Figure 15 shows the changes in the resultant amplitudes of the magnetic anomalies corresponding to defects located at different depths from the surface when eddy currents are excited at different frequencies. At low frequencies, the eddy current induced in the conductor stack has a low amplitude and hence the amplitude of the magnetic anomaly associated with the defect is also low. As the excitation frequency increases, the amplitude of the eddy current induced on the surface increases monotonically; however, owing to the skin effect, the amplitude of the eddy currents flowing in the neighbourhood of the defect increases initially, reaches a maximum at the optimum excitation frequency and decreases steadily thereafter. At higher frequencies, the eddy current tends to be concentrated at the upper surface of the material due to the skin effect. Therefore, the amplitude of the magnetic anomaly due to presence of the defect at a greater depth decreases when higher excitation frequencies are used. The excitation frequencies were varied in steps of 10 Hz for defects at greater depths and 20 Hz for defects at lower depths. The experimental parameters such as lift-off distance, excitation coil current, FLL electronics gain, scanning speed, step size, time constant of the lock in amplifier, etc. were kept constant for the entire series of experiments. The frequency at which the amplitude of the measured magnetic anomaly reaches a maximum value is taken to be the optimum frequency of excitation for the defect located at a particular depth. As a result of these detailed experimental studies, the optimum excitation frequencies have been estimated for the defects located at different depths from the surface, and are listed in Table 2. As shown in Figure 16, the square root of the optimum excitation frequency is found to be inversely proportional to the defect depth.

For defects at lower depths from the surface, the signal-to-noise ratio is excellent for a wide range of frequencies; for defects at greater depths from the surface, however, the range of frequencies which can be used for defect detection becomes narrow due to poor signal-to-noise ratio and skin effect of the conducting materials. It may also be noted that such defects can be detected only using SQUID-based system for NDE.

This system has also been used for tracking the progressive transformation of the extremely low content magnetic δ-ferrite phase into non-magnetic phases in the 316L(N) stainless-steel weldment specimens subjected to LCF at high temperatures. 316L(N) stainless-steel weldment specimens were prepared by welding 316L(N) base metal with 316N electrodes by manual metal-arc welding process. Welding was carried out on a 25 mm thick plate with a double-V configuration and with an included angle of 70°. Welds were radio-graphed and only sound joints were taken for fabrication of the specimens. LCF tests were conducted

Table 2. Optimum excitation frequencies for the defect at different depths

Depth (mm)	2	4	6	8	10	12	14
f_{opt} (Hz)	453	313	233	183	143	123	103

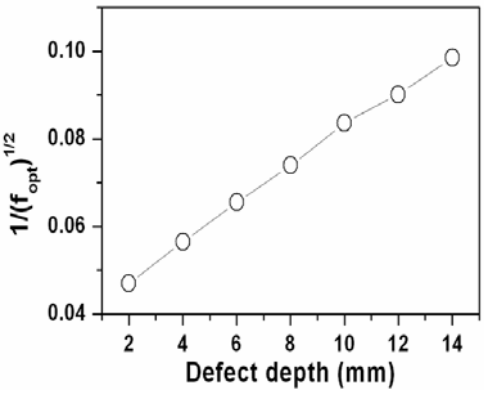

Figure 16. Variation of optimum excitation frequency with defect depth.

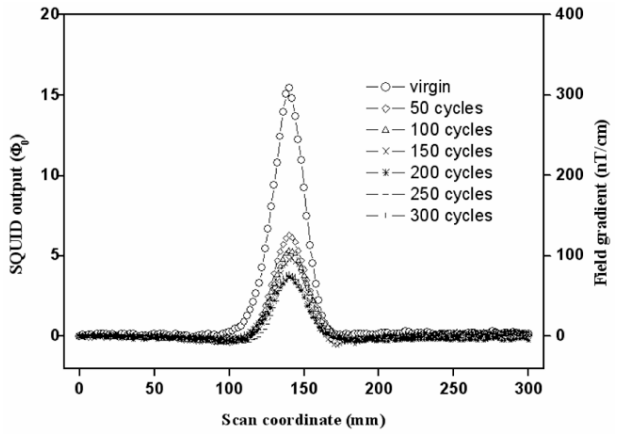

Figure 17. SQUID output for the virgin and fatigue cycled weldment specimen.

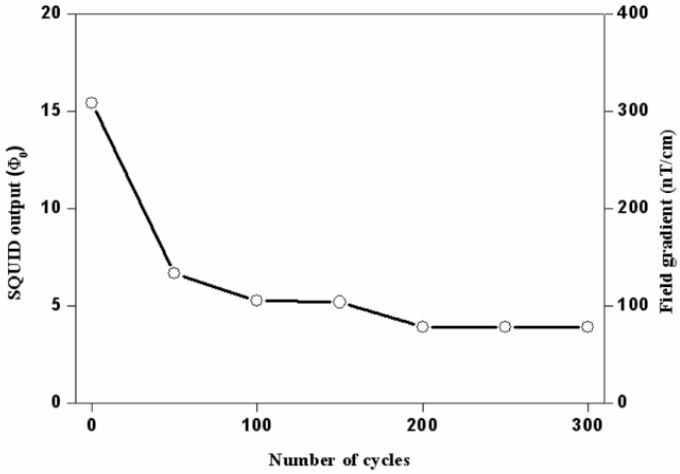

Figure 18. SQUID output versus number of fatigue cycles for the weldment specimen subjected to fatigue deformation at 600°C.

at a strain amplitude of ±0.6% using an Instron servohydraulic fatigue testing machine under total axial strain control mode at 600°C. A strain rate of $3 \times 10^{-3}\ s^{-1}$ was employed for the test. As the sample was scanned under the cryostat, the SQUID output revealed a characteristic magnetic anomaly when the centre of the gauge length of the sample passed under the pick-up loop, indicating the presence of a magnetic phase at the location of the weld.

A series of experiments has been carried out in the stainless-steel weldment specimens to evaluate the transformation of magnetic phase to non-magnetic phases at different levels of fatigue deformation. In this study a single weld joint was selected for remanent magnetization measurements in the virgin state and subsequently after every 50 fatigue cycles. At every stage prior to fatigue cycling and remanent magnetization measurement, the weld joint was properly demagnetized by subjecting it to low-frequency alternating magnetic field to eliminate the influence of the past history and then re-magnetized by applying a preset DC magnetizing field (35 Oe) for a preset time (300 s) before measurement of remanent magnetization using SQUID-based set-up commenced. The peak value of the demagnetization field was kept slightly higher than the magnetizing field. To evaluate the relative changes in the magnetic content of the weldment specimen, the parameters of the measurement set-up such as stand-off distance, FLL gain, etc. were maintained constant throughout the whole series of measurements. The virgin weldment specimen gave a maximum SQUID signal of $15\Phi_0$, which decreased rapidly to $6.67\Phi_0$ when the sample was subjected to LCF for 50 cycles. Thereafter, no significant changes in the maximum SQUID signal could be observed up to 150 cycles. However, a marked decrease in SQUID signal was noticed when the sample was subjected to LCF for 200 cycles accompanied by the initiation of a crack at the boundary of the weldment specimen. Micro-cracks were seen at the boundary of the weldment specimen when it was examined using a microscope. The magnetic profile of the weldment specimen scanned under the SQUID probe is shown in Figure 17 in the virgin state as well as after subjecting it to different levels of fatigue deformation. Figure 18 shows the variation in maximum SQUID signal as a function of the number of cycles of fatigue loading, and portrays the transformation of magnetic δ-ferrite to non-magnetic phases when the weldment specimen is subjected to LCF at 600°C. It may be noted that although the initial signals were large, SQUID-based measurements were

intended to look for small magnetic anomalies, if any, which could be correlated with the residual life of the weldment specimen.

Conclusion

The development of a high-field SQUID magnetometer and a SQUID-based NDE system has been described. The SQUID magnetometer has a sensitivity of 1.2×10^{-7} emu and has been calibrated using YIG sphere as a standard reference material. After calibration, the system performance has been further evaluated by estimating the effective magnetic moment of Gd^{3+} through temperature-dependent magnetization measurements of standard Gd_2O_3 samples. A SQUID-based system for NDE using a precision *XY* scanner and a computer-controlled data-acquisition system has been developed. The system has been used to detect subsurface defects in relatively thick conducting plates, which are not ordinarily detectable by conventional eddy current techniques owing to the skin depth limitations. A set of aluminum plates free from defects and an aluminum plate with an artificially engineered defect have been fabricated to systematically study the shape and amplitude of the magnetic anomalies associated with the defect as a function of frequency and defect depth. The results of this comprehensive series of studies have been used to determine the optimum frequency of eddy current excitation depending on the defect depth. The experimental results are likely to provide useful guidance on the selection of appropriate excitation frequencies for the detection of subsurface flaws. Possibilities exist for the use of data for a reliable inference on the defect depth. The system has also been used to characterize the δ-ferrite content in SS 316L(N) weldment specimen subjected to fatigue at 600°C. The ability of the system to detect very small changes in remanent magnetization makes it possible to identify small magnetic anomalies, if any, prior to the complete failure of the weld. Possibilities exist for developing the technique further to forecast the residual life of a weld undergoing fatigue damage.

1. Clarke, J., In *The New Superconducting Electronics* (eds Weinstock, H. and Ralston, R. W.), Kluwer, Dordrecht, 1993, pp. 123–180.
2. Koch, H., In *Sensors – A Comprehensive Survey* (eds Boll, R. and Overshott, K. J.), VCH Publishers, NY, 1989, vol. 5, pp. 381–445.
3. Clarke, J., Goubau, W. M. and Ketchen, M. B., *J. Low Temp. Phys.*, 1976, **25**, 99–144.
4. Jaycox, J. M. and Ketchen, M. B., *IEEE Trans. Magn.*, 1981, **17**, 401–403.
5. Nagendran, R., Thirumurugan, N., Chinnasamy, N., Janawadkar, M. P. and Sundar, C. S., *Rev. Sci. Instrum.*, 2011, **82**, 015109.
6. Gramm, K., Lundgren, L. and Beckman, O., *Phys. Scr*., 1976, **13**(2), 93–95.
7. Magnusson, J., Djurberg, C., Granberg, P. and Nordblad, P., *Rev. Sci. Instrum*., 1997, **68**, 3761.
8. Beauvillain, P., Chappert, C. and Renard, J. P., *J. Phys. E: Sci. Instrum.*, 1985, **18**, 839–845.
9. Vitale, S., Morante, S. and Cerdonio, M., *Rev. Sci. Instrum.*, 1982, **53**(2), 1123–1128.
10. Philo, J. S. and Fairbank, W. M., *Rev. Sci. Instrum.*, 1977, **48**(12), 1529–1536.
11. Tsoy, G., Janu, Z., Novak, M., Soukup, F. and Tichy, R., *Physica B*, 2000, **284–288**, 2122–2123.
12. Blank, D. H. A., ter Brake, H. J. M. and Flokstra, J., SQUID 85. In Proceedings of the Third International Conference on Superconducting Quantum Devices, Berlin (West) (eds Hahlbohm, H. D. and Lubbig, H.), 25–28 June 1985, pp. 859–864.
13. Jackson, T. J., Keene, M. N. and Gough, C. E., *Meas. Sci. Technol.*, 1992, **3**, 988–991.
14. Ishizuka, M. and Tohi, Y., *Jpn. J. Appl. Phys*., 1980, **19**(4), 639–646.
15. Tuset, E. D., Sagdahl, L. T., Karkut, M. G. and Fossheim, K., *Physica C*, 1994, **235–240**, 2927–2928.
16. Kohl, M. and Harrison, J. P., *Cryogenics*, 1991, **31**, 369–372.
17. Pelizzone, M. and Treyvaud, A., *Appl. Phys*., 1981, **24**, 375–379.
18. Genna, J. C. *et al.*, *Rev. Sci. Instrum.*, 1991, **62**, 1824–1827.
19. Nagendran, R., Thirumurugan, N., Chinnasamy, N., Janawadkar, M. P. and Sundar, C. S., *Rev. Sci. Instrum.*, 2010, **81**, 045112.
20. Jenks, W. G., Sadeghi, S. S. H. and Wikswo, J. P., *J. Phys. D*., 1997, **30**, 293–323.
21. Tavrin, Y., Siegel, M. and Hinken, J. H., *IEEE Trans. Appl. Supercond*., 1999, **9**, 3809–3812.
22. Chen, P., Chen, L., Li, J. and Ong, C. K., *Supercond. Sci. Technol.*, 2002, **15**, 855–858.
23. Harold Weinstock, *IEEE Trans. Magn.*, 1991, **27**, 3231–3236.
24. Mück, M., Korn, M., Welzel, C., Grawunder, S. and Schölz, F., *IEEE Trans. Appl. Supercond.*, 2005, **AS–15**, 733–736.
25. Klein, U. *et al.*, *IEEE Trans. Appl. Supercond*., 1997, **7**, 3037–3039.
26. Nagendran, R. *et al.*, *IEEE Trans. Appl. Supercond*., 2007, **17**(3), 3824–3829.
27. Nagendran, R. *et al.*, *NDT&E Int.*, 2007, **40**(3), 215–219.

ACKNOWLEDGEMENT. We thank Dr C. S. Sundar, Dr Y. Hariharan and Dr Baldev Raj for support during the development of SQUID-based measuring systems.

Received 16 May 2011; accepted 28 July 2011

R. Nagendran, N. Thirumurugan, N. Chinnasamy and M. P. Janawadkar are in the Condensed Matter Physics Division, Materials Science Group, Indira Gandhi Centre for Atomic Research, Kalpakkam 603 102, India.*
**e-mail: nags@igcar.gov.in*